



A simplified model of thin layer static/flowing dynamics for granular materials with yield

Christelle Lusso, François Bouchut, Alexandre Ern, Anne Mangeney

► To cite this version:

Christelle Lusso, François Bouchut, Alexandre Ern, Anne Mangeney. A simplified model of thin layer static/flowing dynamics for granular materials with yield. 2014. hal-00992309v1

HAL Id: hal-00992309

<https://hal.science/hal-00992309v1>

Preprint submitted on 16 May 2014 (v1), last revised 7 Apr 2017 (v4)

HAL is a multi-disciplinary open access archive for the deposit and dissemination of scientific research documents, whether they are published or not. The documents may come from teaching and research institutions in France or abroad, or from public or private research centers.

L'archive ouverte pluridisciplinaire **HAL**, est destinée au dépôt et à la diffusion de documents scientifiques de niveau recherche, publiés ou non, émanant des établissements d'enseignement et de recherche français ou étrangers, des laboratoires publics ou privés.

A simplified model of thin layer static/flowing dynamics for granular materials with yield

Christelle Lusso¹, François Bouchut², Alexandre Ern¹, Anne Mangeney^{3,4}

May 16, 2014

¹Université Paris-Est, CERMICS (ENPC),
F-77455, Marne-la-Vallée, France

²Université Paris-Est, Laboratoire d'Analyse et de Mathématiques Appliquées (UMR 8050),
CNRS, UPEM, UPEC, F-77454, Marne-la-Vallée, France

³Université Paris Diderot, Sorbonne Paris Cité, Institut de Physique du Globe de Paris,
Seismology group, 1 rue Jussieu, 75005 Paris, France,

⁴ANGE team, INRIA, CETMEF, Lab. J.-L. Lions, Paris, France

Abstract

We introduce a simplified model for thin layer flows of granular materials with yield. The model is derived from a Drucker–Prager rheology, and describes the dynamics of the velocity profile and of the transition between static and flowing material. We compare the analytical solution in the inviscid case, and the numerical solution in the viscous case, to experimental data. Although the model does not describe the variations in the flow direction, it is able to reproduce essential features of granular flows experiments over an inclined static layer of grains, such as the stopping time and the erosion of the initial static bed, which is shown to depend on the viscosity.

KEYWORDS. Granular materials, static/flowing transition, thin layer flow, interface dynamics, velocity profile, erosion, stopping time

1 Introduction

The understanding and theoretical description of the static/flowing transition in dense granular flows is a central issue in research on granular materials, with strong implications for industry and geophysics, in particular in the study of natural gravity-driven flows. These flows (e.g., landslides or debris avalanches) play a key role in erosion processes on the Earth's surface and represent a major origin of natural hazard. In recent years, significant progress in the mathematical, physical, and numerical modelling of gravitational flows has made it possible to develop and use numerical models to investigate geomorphological processes and assess risks related to such natural hazards. However, severe limitations prevent us from fully understanding the physical processes acting in natural flows and from predicting landslide dynamics and deposition [e.g., Lucas et al., 2014]. In particular, a major challenge in numerical models is to describe accurately complex natural phenomena such as the static/flowing transition in granular flows.

Geophysical, geotechnical, and physical studies have shown that the static/flowing transition related to the existence of no-flow and flow zones within the mass plays a crucial role in most granular flows and provides a key to understanding their dynamics in a natural context. This transition occurs in erosion/deposition processes when a layer of particles is flowing over a static layer or near the destabilization and arrest phases. Indeed, natural flows often travel on deposits of past events made or not of the same grains, and entrain material from the



Figure 1: Deposits of a succession of gravitational flows on the slope of the Soufriere Hill volcano, Montserrat, Lesser Antilles, showing clear or more diffuse interfaces between the deposits of different events (Picture Anne Mangeney and Maxime Farin during a field trip with Eliza Calder, Paul Cole and Paddy Smith).

initially static bed (Figure 1). Even though field measurements of erosion processes are very difficult [e.g., Conway et al., 2010; Berger et al., 2011; Weidinger et al., 2014], entrainment of underlying material is known to significantly change the flow dynamics and deposit [e.g., Hungr et al., 2001; Sovilla et al., 2006; Mangeney et al., 2007; Crosta et al., 2009a; Mangeney et al., 2010].

Experimental studies have provided some answers to the static/flowing transition in granular flows, showing for example that the presence of a very thin layer of erodible material lying on an inclined bed may increase the maximum running distance of a granular avalanche flowing down the slope by up to 40% and change the flow regimes [Mangeney et al., 2010; Iverson et al., 2011; Farin et al., 2014]. In these experiments, that mimic natural flows over initially static beds (Figure 2), quasi-uniform flows develop when the slope angle θ is a few degrees lower than the typical friction angle δ of the involved material [Farin et al., 2014]. The change in time of the static/flowing interface b and of the velocity profiles $U(Z)$ within the granular mass, where Z is the direction normal to the bed, have been measured (Figures 3 and 4 respectively). At a given position X along the plane, the flow is shown to excavate the initially static layer immediately when the front reaches this position. The static/flowing interface rapidly penetrates into the static layer, stabilizing at an almost constant value for significantly high slopes, and then rising up linearly or exponentially toward the free surface until the stopping of the whole material (Figure 3). A theoretical description of these observations is still lacking. In particular, the questions are what controls the change in time of the static/flowing interface, of the velocity profiles, etc. and how are they related to the rheology of the granular material and to the initial and boundary conditions.

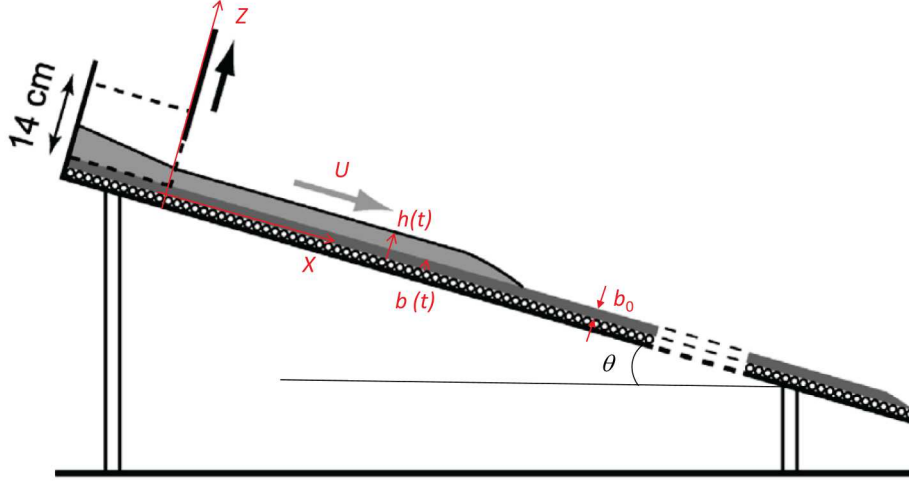


Figure 2: Experimental setup from [Mangeney et al., 2010] and [Farin et al., 2014] of granular column collapse over inclined planes covered by an initially static layer made of the same grains as those released in the column. For slope angles θ a few degrees smaller than the typical friction angle δ of the involved material, a quasi-uniform flow develops behind the front.

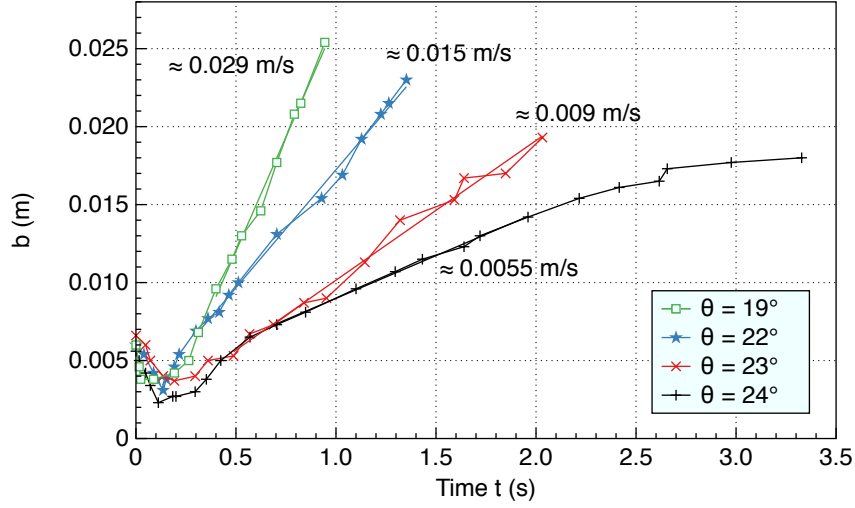


Figure 3: Position of the static/flowing interface b as a function of time t until the stopping of the granular mass, measured at $X = 90\text{cm}$ from the gate, in experimental granular collapse over an initially static granular layer of thickness $b^0 = 5\text{mm}$ over an inclined channel of slope $\theta = 19^\circ$ (green squares), $\theta = 22^\circ$ (blue stars), $\theta = 23^\circ$ (red crosses), and $\theta = 24^\circ$ (black vertical crosses). Time $t = 0\text{s}$ corresponds to the time when the front of the flowing layer reaches the position $X = 90\text{cm}$. The approximate upward velocity of the static/flowing transition is indicated in m/s for each slope angle. Results extracted from the experiments of [Farin et al., 2014] for granular columns of initial radius $r_0 = 20\text{cm}$, initial thickness $h_0 = 14\text{cm}$, and width $W = 20\text{cm}$ (i.e., volume $V = 5600\text{cm}^3$).

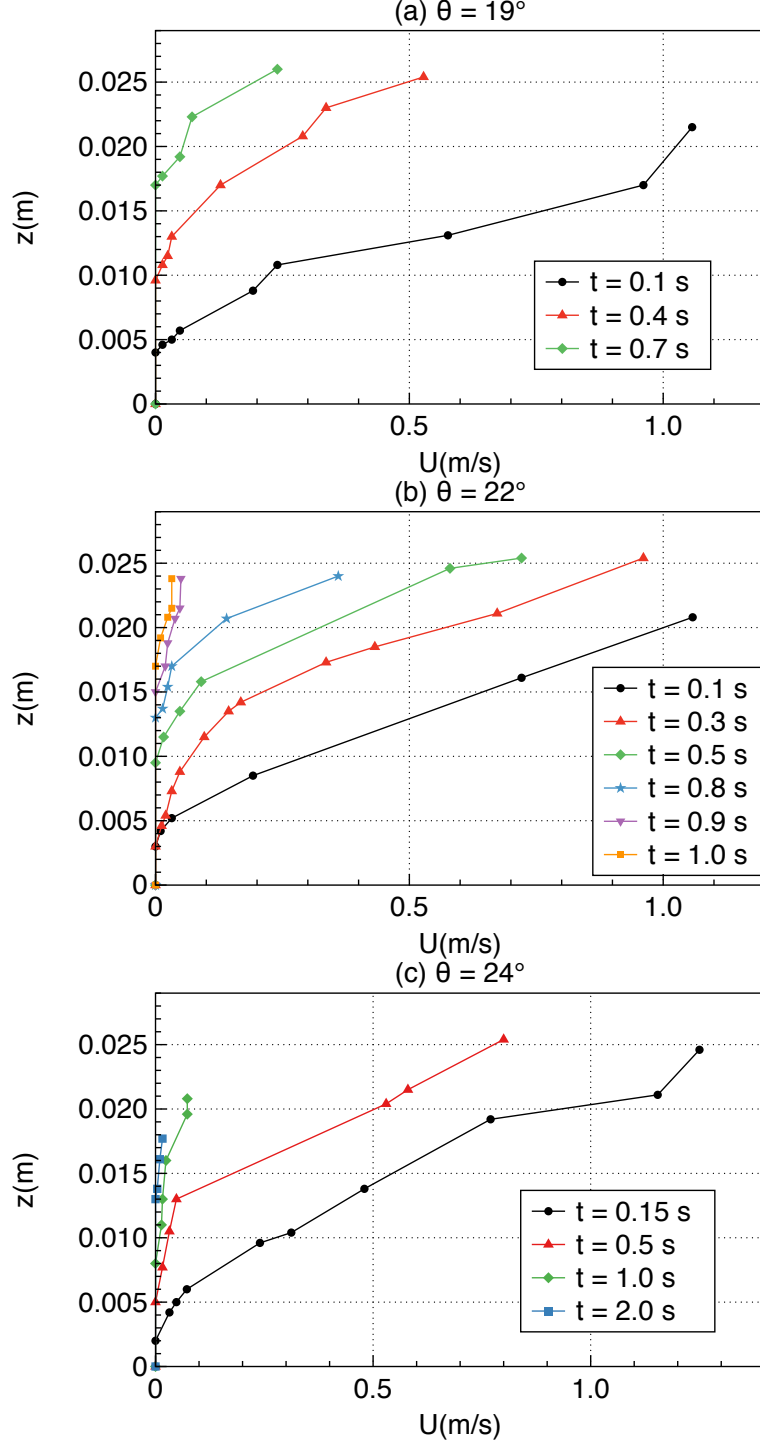


Figure 4: Velocity profiles $U(Z)$ at different times until the stopping of the granular mass, measured at $X = 90\text{cm}$ from the gate, in experiments of granular collapse over an initially static granular layer of thickness $b^0 = 5\text{mm}$ over an inclined channel of slope (a) $\theta = 19^\circ$, (b) $\theta = 22^\circ$, and (c) $\theta = 24^\circ$. Time $t = 0\text{s}$ corresponds to the time when the front of the flowing layer reaches the position $X = 90\text{cm}$. Results extracted from the experiments of [Farin et al., 2014] for granular columns of initial radius $r_0 = 20\text{cm}$, initial thickness $h_0 = 14\text{cm}$, and width $W = 20\text{cm}$ (i.e., volume $V = 5600\text{cm}^3$).

To alleviate the high computational costs related to the description of the real topography, that plays a key role in natural flow dynamics, thin layer (i.e., the thickness of the flow is assumed to be small compared to its downslope extension) depth-averaged models are generally used to simulate landslides [Savage and Hutter, 1989]. Rigorous derivation of these models over arbitrary topography was provided, but the static/flowing transition is generally neglected [e.g., Bouchut et al., 2003; Bouchut and Westdickenberg, 2004; Mangeney-Castelnau et al., 2005]. Several attempts have been made to describe this transition in thin layer (i.e., shallow) models, in particular by deriving an equation for the static/flowing interface or by prescribing the erosion/deposition rates [e.g., Khakhar et al., 2001; Iverson, 2012]. However, these approaches are generally based on debatable phenomenological laws and/or are too schematic to be extended to natural flows over real topography. In particular, the simplifications used in some previous models lead to a non-consistent energy equation [Bouchut et al., 2008]. Better understanding of the non-averaged case will certainly help defining more physically relevant depth-averaged models including the static/flowing transition.

Recent works have shown that viscoplastic flow laws describe well granular flows and deposits in different regimes from steady uniform flows [GDR-MiDi, 2004; Silbert et al., 2001; Jop et al., 2005, 2006] to transient granular collapse over rigid or erodible horizontal beds [Crosta et al., 2009b; Lagr  e et al., 2011] and inclined beds [Ionescu et al., 2014]. The quasi-static regime near the static/flowing interface is known to be very complex, involving strong and weak force chains and local rearrangement of particles [e.g., Deboeuf et al., 2005; Richard et al., 2008]. This regime is not accurately described by these viscoplastic laws involving a simple yield stress. The questions are however whether such ‘simple’ viscoplastic laws are able to describe quantitatively the change in time of the static/flowing interface and of the velocity profiles observed experimentally for flows over an initially static bed and how the viscosity affects these processes.

We propose here a mathematical model for describing the static/flowing interface evolution in a dry granular material. It is derived from the shallow expansion performed in [Bouchut et al., 2014], using a viscoplastic Drucker–Prager rheology with yield stress. Even if the flow is assumed to be shallow, the normal variable Z is still present in the model. The formulation involves an extra boundary condition at the static/flowing interface $Z = b(t)$, that determines its time evolution. The effects of gravity and internal friction are taken into account in a source term S . The main simplification in our model is that we remove the flow-parallel variable X that is present in [Bouchut et al., 2014], and that plays a key role in real flows, taking into account the topography and inflow information. Thus, we assume here a uniform flow ($h = cst$) over a flat inclined plane ($\theta = cst$). The analysis of this simple system provides new insight into the change in time of the static/flowing interface and of the velocity profiles. The model is introduced in Section 2. Then, we derive an analytical solution in the inviscid case with a constant source term (Section 3) that partly reproduces the experimental observations and shows explicitly how the static/flowing interface and the velocity profiles are related to the flow characteristics and to the initial and boundary conditions. The numerical simulation of the viscous model shows that, contrary to the inviscid case, viscosity makes it possible to reproduce the initial penetration of the static/flowing interface within the static bed and the exponential shape of the velocity profiles near this interface (Section 4). Finally, these results are discussed based on comparison with former experimental and numerical studies on granular flows, showing the key ingredients and the limits of this shallow viscoplastic model to provide new understanding and modelling of laboratory and natural flows (Section 5).

2 A simplified model with source term and moving interface

2.1 Origin of the model

A shallow model for yield viscoplastic flows with static/flowing transition has been derived in [Bouchut et al., 2014]. It is formulated in the variables X in the direction tangent to the topography, and Z normal to it. The topography is described by its angle $\theta(X)$ with the horizontal (Figure 5 in the case of a flat topography). Then, a formal expansion of the governing equations for an incompressible viscoplastic flow with Drucker–Prager rheology leads to the momentum balance equation

$$\partial_t U + S - \nu \partial_{ZZ}^2 U = 0 \quad \text{for all } Z \in (b, h), \quad (2.1)$$

where $U(t, X, Z)$ is the velocity in the direction tangent to the topography, and $\nu \geq 0$ is the kinematic viscosity. In (2.1), $h(t, X)$ is the thickness of the layer, and $b(t, X)$ is the position of the interface between the static part $Z < b(t, X)$ (where we set $U \equiv 0$) and the flowing part $Z > b(t, X)$. The thickness h evolves according to a kinematic free-surface condition, and the evolution of the interface b is implicitly governed by the boundary conditions for all $t > 0$,

$$U = 0 \quad \text{at } Z = b, \quad (2.2a)$$

$$\nu \partial_Z U = 0 \quad \text{at } Z = b, \quad (2.2b)$$

$$\nu \partial_Z U = 0 \quad \text{at } Z = h. \quad (2.2c)$$

Knowing that the material is at rest in the part below the interface, these boundary conditions mean that the velocity is continuously differentiable through the interface (in the viscous case). Moreover, the viscous stress vanishes at the free surface $Z = h$.

The source S in (2.1) depends on t, X, Z and is expressed as

$$S = g(-\sin \theta + \partial_X(h \cos \theta)) - \mu \partial_Z p \quad \text{for all } Z \in (b, h), \quad (2.3)$$

where $g > 0$ is the gravity acceleration, $\mu = \tan \delta > 0$ is the friction coefficient with δ the friction angle related to the material, and $p(t, X, Z)$ is the pressure. This pressure has an asymptotic nonlinear expression in terms of $\partial_X U$ and $\partial_Z U$, but the particular form of this expression is irrelevant here. The expression (2.3) is valid in the context of positive angle θ (note that this convention differs from [Bouchut et al., 2014]) and of a (strictly) increasing velocity profile in the flowing layer, i.e., $\partial_Z U > 0$ for all $Z \in (b, h)$.

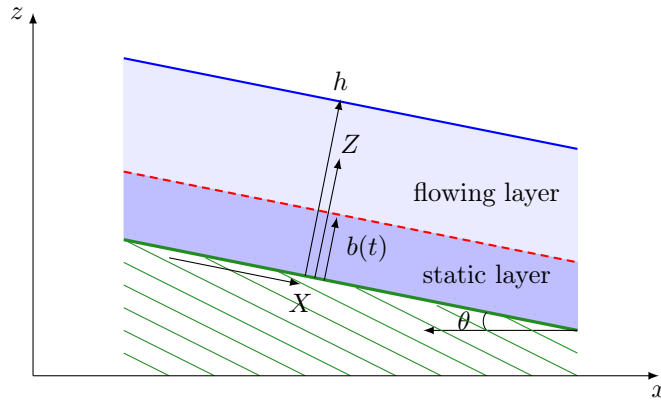


Figure 5: Simplified flow configuration consisting of a uniform flowing layer over a uniform static layer, both parallel to the rigid bed of slope angle θ . The static/flowing interface is $b(t)$, and the total thickness of the mass h is constant.

2.2 The simplified model

The motivation of our simplified model stems from the fact that the system (2.1), (2.2) involves the dependency on X of the unknowns only via the thickness of the layer h and the source term S , or equivalently via the expression of the pressure, because of (2.3). In other words, if the source S and the thickness of the layer h are known, the system (2.1), (2.2) can be considered as a system in the variables t, Z , while X is only a parameter.

Therefore, our simplified model with moving interface considers that (at fixed X , and we thus omit the variable X) the source is given empirically as a function $S(t, Z)$. The angle $\theta > 0$ is then constant, and we assume also that h is independent of time, and therefore constant. Our system reduces then to finding $U(t, Z)$ for $b(t) < Z < h$, and $b(t)$ satisfying $0 < b(t) < h$, such that

$$\partial_t U(t, Z) + S(t, Z) - \nu \partial_{ZZ}^2 U(t, Z) = 0 \quad \text{for all } Z \in (b(t), h), \quad (2.4)$$

with the boundary conditions for all $t > 0$,

$$U = 0 \quad \text{at } Z = b(t), \quad (2.5a)$$

$$\nu \partial_Z U = 0 \quad \text{at } Z = b(t), \quad (2.5b)$$

$$\nu \partial_Z U = 0 \quad \text{at } Z = h. \quad (2.5c)$$

We assume that $S(t, Z)$ is defined for $Z \in [0, h]$ and is continuous in time and space. Finally, we specify a continuous velocity profile $U^0(Z)$ defined for $Z \in [0, h]$, such that for some $b^0 \in (0, h)$ (initial position of the interface), the function U^0 satisfies $U^0(Z) = 0$ for $Z \in [0, b^0]$, and $\partial_Z U^0 > 0$ for $Z \in (b^0, h)$. The initial condition on the velocity is then formulated as

$$U(0, Z) = U^0(Z) \quad \text{for all } Z \in [0, h], \quad (2.6)$$

where $U(0, Z)$ is the limit as $t \downarrow 0$ of $U(t, Z)$ extended by 0 for $Z < b(t)$.

We remark that if we take an hydrostatic pressure $p = g \cos \theta (h - Z)$ in (2.3), neglecting the derivative in X (we recall that X has been considered as a parameter, which does not mean that the quantities are independent of X), we infer that S is constant in time (and uniform in space) with

$$S = g(-\sin \theta + \mu \cos \theta). \quad (2.7)$$

The source term is thus the result of the balance between the driving force due to gravity ($g \sin \theta > 0$) and the friction force ($\mu g \cos \theta > 0$). Indeed, in the case of (2.7), according to [Bouchut et al., 2014; Lusso, 2013], the solution of the system (2.4), (2.5), (2.6) is an exact solution to the two-dimensional Drucker–Prager model without dependency in X .

2.3 Properties of the model

The simplified model (2.4), (2.5), (2.6) enjoys several interesting properties; for more insight into their proof, we refer to [Lusso, 2013]. We make the assumptions stated in Subsection 2.2 on the initial data.

- Monotonicity of the velocity profile. Assume that $\nu > 0$ and that the source term is decreasing in space

$$\partial_Z S(t, Z) \leq 0 \quad \text{for all } t \geq 0, \text{ and all } Z \in [0, h]. \quad (2.8)$$

Condition (2.8) can be interpreted as a stability condition. Recalling (2.3), this condition can also be stated as a convexity property for the pressure, i.e., $\partial_{ZZ}^2 p \geq 0$. The stability condition (2.8) is obviously satisfied if the source term is uniform in space. Then, under the above assumptions, for all $t \geq 0$, and as long as $0 < b(t) < h$, the following holds:

$$\partial_Z U(t, Z) > 0 \quad \text{for all } Z \in (b(t), h). \quad (2.9)$$

Moreover, the source term is nonnegative at the interface

$$S(t, b(t)) \geq 0 \quad \text{for all } t > 0. \quad (2.10)$$

This last property is obtained by differentiating in time (2.5a), which yields

$$\partial_t U(t, b(t)) + \partial_Z U(t, b(t)) \dot{b}(t) = 0. \quad (2.11)$$

Since $\nu \neq 0$, the condition (2.5b) leads to $\partial_t U(t, b(t)) = 0$. Then, evaluating (2.4) at $Z = b(t)$, we infer that

$$S(t, b(t)) = \nu \partial_{ZZ}^2 U(t, b(t)). \quad (2.12)$$

Owing to (2.9) and using again (2.5b), we obtain $\partial_{ZZ}^2 U(t, b(t)) = \lim_{Z \downarrow b(t)} \partial_Z U(t, Z) / (Z - b(t)) \geq 0$, whence the result (2.10).

In the case $\nu = 0$, we impose (2.10) as an additional condition in the simplified model. This additional condition can be interpreted as an entropy condition in the limit of vanishing viscosity.

We observe that in the case (2.7) of constant source, the condition (2.10) implies that $\tan \theta \leq \mu$, saying that the internal friction must at least neutralize the gravity force due to the slope. This is a necessary condition for a solution to the model with moving interface (2.4), (2.5), (2.6) to exist. Indeed, if this condition is not satisfied, we expect that “ $b = 0$ ”, meaning that all the layer flows down.

- We can formally derive a differential equation for the time evolution of the position of the interface. If $\nu > 0$ and $S(t, b(t)) \neq 0$, then

$$\dot{b}(t) = \left(\frac{\partial_Z S(t, b(t)) - \nu \partial_{ZZZ}^3 U(t, b(t))}{S(t, b(t))} \right) \nu. \quad (2.13)$$

If $\nu = 0$ and $\partial_Z U(t, b(t)) \neq 0$, then

$$\dot{b}(t) = \frac{S(t, b(t))}{\partial_Z U(t, b(t))}. \quad (2.14)$$

3 Analytical solution in the inviscid case with a constant and uniform source term

3.1 Analytical solution

In the inviscid case $\nu = 0$, the simplified model (2.4), (2.5), (2.6) can be written

$$\partial_t U(t, Z) + S(t, Z) = 0 \quad \text{for all } Z \in (b(t), h), \quad (3.1)$$

with the boundary condition for all $t > 0$,

$$U(t, b(t)) = 0, \quad (3.2)$$

the initial condition (2.6), and the entropy condition (2.10). Moreover, if the source term is chosen constant and uniform as in (2.7), i.e.,

$$S(t, Z) = S := g \cos \theta (\tan \delta - \tan \theta) \geq 0, \quad (3.3)$$

with $\mu = \tan \delta$, $\theta \leq \delta$, then we can infer an analytical solution. Specifically, the solution to (3.1), (3.2), (2.6) is given by

$$U(t, Z) = \max \left(U^0(Z) - St, 0 \right) \quad \text{for all } Z \in [0, h]. \quad (3.4)$$

Equation (3.4) shows that the velocity profile (at all times when a flowing layer exists) has the same shape as the initial velocity profile: it is just shifted towards decreasing velocities with a constant speed S , and clipped below the value 0. Note that the velocity profile only depends on g , θ , δ through S in (3.3). If $S = 0$, the solution is steady, while if $S > 0$, the velocity decreases with time, until the stopping of the flow. Furthermore, the interface $b(t)$ results from the following implicit equation:

$$U^0(b(t)) = St. \quad (3.5)$$

This equation has a unique solution in $[b^0, h]$ for all times $t \leq t^{\text{stop}}$, with t^{stop} defined by

$$t^{\text{stop}} = \frac{U^0(h)}{S} = \frac{U^0(h)}{g \cos \theta (\tan \delta - \tan \theta)}. \quad (3.6)$$

The complete stopping of the flow occurs at $t = t^{\text{stop}}$. For all times $t > t^{\text{stop}}$, the velocity U can be extended by setting $U(t, Z) = 0$ for all $Z \in [0, h]$, and $b(t) = h$.

3.2 Choice of the parameters and initial conditions

In order to compare the analytical solution to the results measured in the experiments of [Farin et al., 2014], we have to prescribe the friction angle δ , the slope angle θ , the thickness of the granular layer h , the thickness of the initially static layer b^0 , and the initial velocity profile $U^0(Z)$. Glass beads of diameter $d \simeq 500\mu\text{m}$ were used in the experiments, with repose and avalanche angles of about 23° and 25° , respectively. Because wall effects are known to increase the effective friction for granular flows in channels as those of Farin et al., 2014, we use here a friction angle of $\delta = 26^\circ$ [Taberlet et al., 2003; Jop et al., 2005]. We perform different tests by varying the slope angle θ from 19° to 24° , while we prescribe $b^0 = 5\text{mm}$, which is the initial static width in the experiments, and $h = 0.02\text{m}$, corresponding to the mean thickness at the position $X = 90\text{cm}$ where the measurements have been performed, see Figure 4. In this section, we always take

$$\delta = 26^\circ, \quad b^0 = 0.005\text{m}, \quad h = 0.02\text{m}. \quad (3.7)$$

The objective here is only to compare the order of magnitude and the general trend of the analytical solution to the experimental results, since the experiments are more complicated than the uniform granular layer and the initial conditions prescribed in the model. In particular, the thickness of the granular layer in the experiments may vary by up to 20% during the flow and slightly depends on the inclination angle (Figure 4). Furthermore, the initial velocity profiles and the maximum velocity also depend on the inclination angle, while we impose here the same velocity profile for all the tests.

Velocity profiles in experimental granular flows have been extensively measured in very different regimes [see e.g., GDR-MiDi, 2004]. For free surface flows over rigid inclined beds, the velocity profiles vary with inclination, thickness of the flow, and time. Essentially, the velocity profiles may vary from a linear profile for thin layers over small slope angles to Bagnold-like profiles for higher inclinations. The same general trend is observed for thicker flows (see Figure 5 of GDR-MiDi, 2004). For surface flows over a pile of static grains, the velocity profiles roughly exhibit an upper linear part in the flowing layer and a lower exponential tail near the static/flowing interface (see Figure 6 of GDR-MiDi, 2004). This is consistent with the measurements shown in Figure 4 from the experiments of Farin et al., 2014. Furthermore, experimental results suggest that the shear rate $\partial_Z U$ is almost constant and equal to $0.5\sqrt{\frac{g}{d}}$ (see e.g., equation (11) of GDR-MiDi, 2004). As a result, for a linear profile of slope α_1 (see case (a) below), we choose $\alpha_1 = 70\text{s}^{-1}$, which is consistent with the velocity profiles measured at $t = 0\text{s}$ in Figure 4.

In order to investigate the different possible profiles of the velocity, we choose three initial velocity profiles defined, for all $Z \in [b^0, h]$, as:

- (a) linear profile $U^0(Z) = \alpha_1(Z - b^0)$, with $\alpha_1 = 70\text{s}^{-1}$,

- (b) exponential profile $U^0(Z) = \alpha_2(e^{\beta Z} - e^{\beta b^0})$, with $\alpha_2 = 0.1\text{m.s}^{-1}$ and $\beta = 130\text{m}^{-1}$,
- (c) Bagnold profile $U^0(Z) = \alpha_3(h^{\frac{3}{2}} - (h + b^0 - Z)^{\frac{3}{2}})$, with $\alpha_3 = 444\text{m}^{-1/2}.\text{s}^{-1}$.

In each case, the maximum velocity is $U^0(h) \simeq 1\text{m.s}^{-1}$. For each profile, equation (2.14) provides explicitly the time evolution of the static/flowing interface as follows:

- (a) $b(t) = \frac{S}{\alpha_1}t + b^0$,
- (b) $b(t) = \frac{1}{\beta} \log \left(\frac{S}{\alpha_2}t + e^{\beta b^0} \right)$,
- (c) $b(t) = h + b^0 - \left(h^{3/2} - \frac{S}{\alpha_3}t \right)^{2/3}$.

These formulae are valid as long as $t \leq t^{\text{stop}} = U^0(h)/S$, i.e., $b(t) \leq h$.

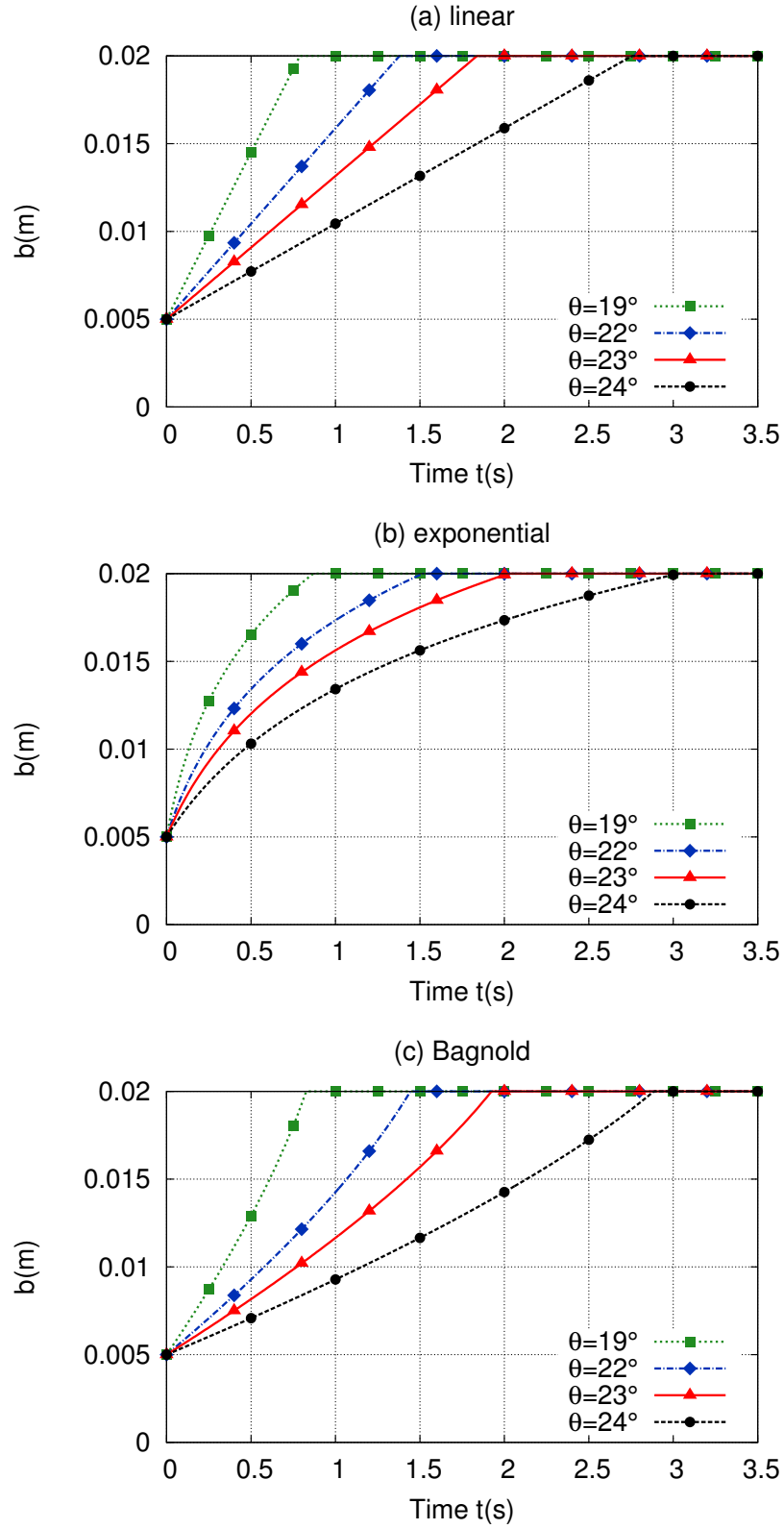


Figure 6: Static/flowing interface b as a function of time t in the inviscid case, for different slope angles and for an initially static granular layer of thickness $b^0 = 5\text{mm}$, using (a) a linear, (b) an exponential, and (c) a Bagnold initial velocity profile.

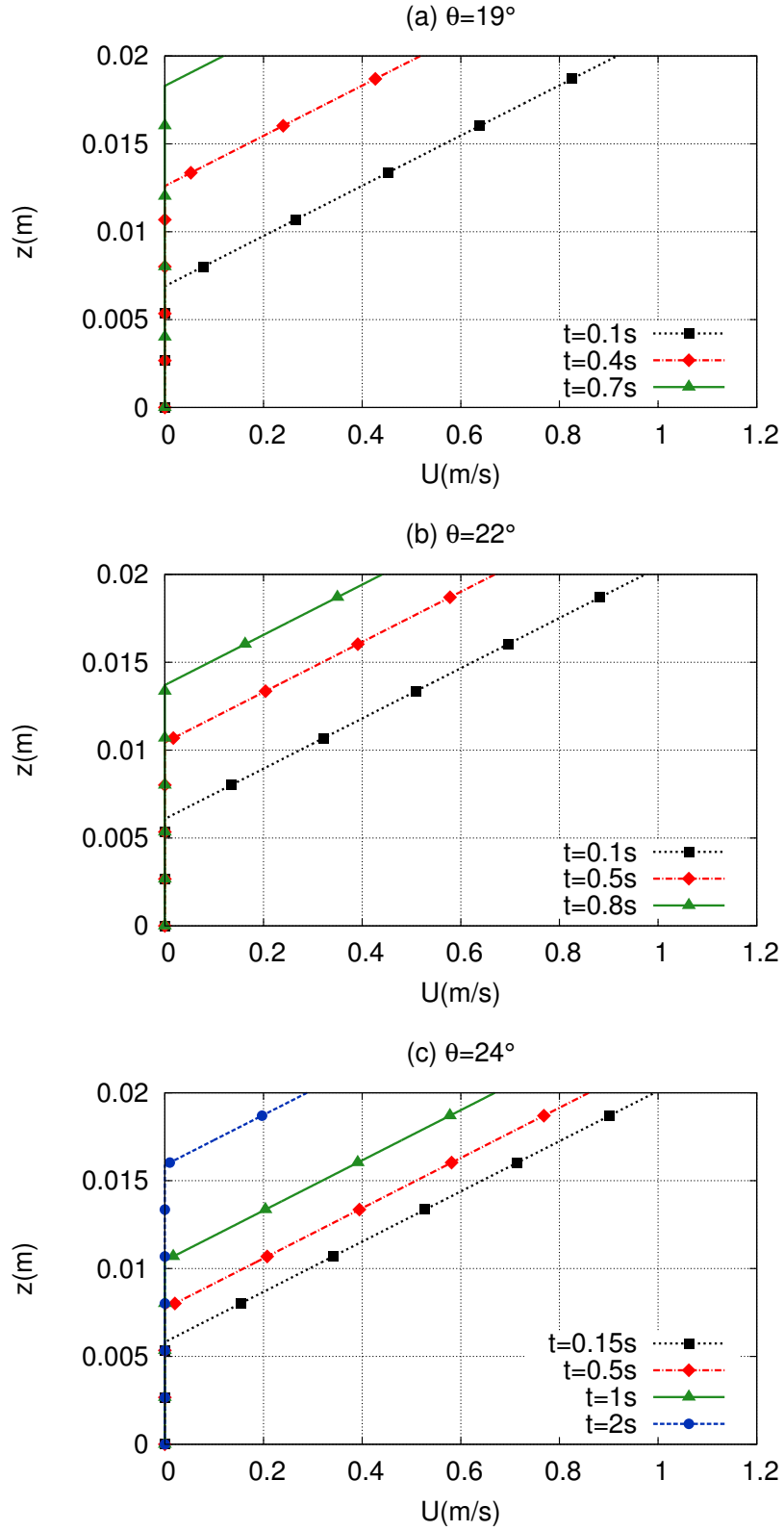


Figure 7: Velocity profiles $U(Z)$ at different times in the inviscid case, with a linear initial velocity profile and an initially static granular layer of thickness $b^0 = 5\text{mm}$ over an inclined plane of slope (a) $\theta = 19^\circ$, (b) $\theta = 22^\circ$, and (c) $\theta = 24^\circ$.

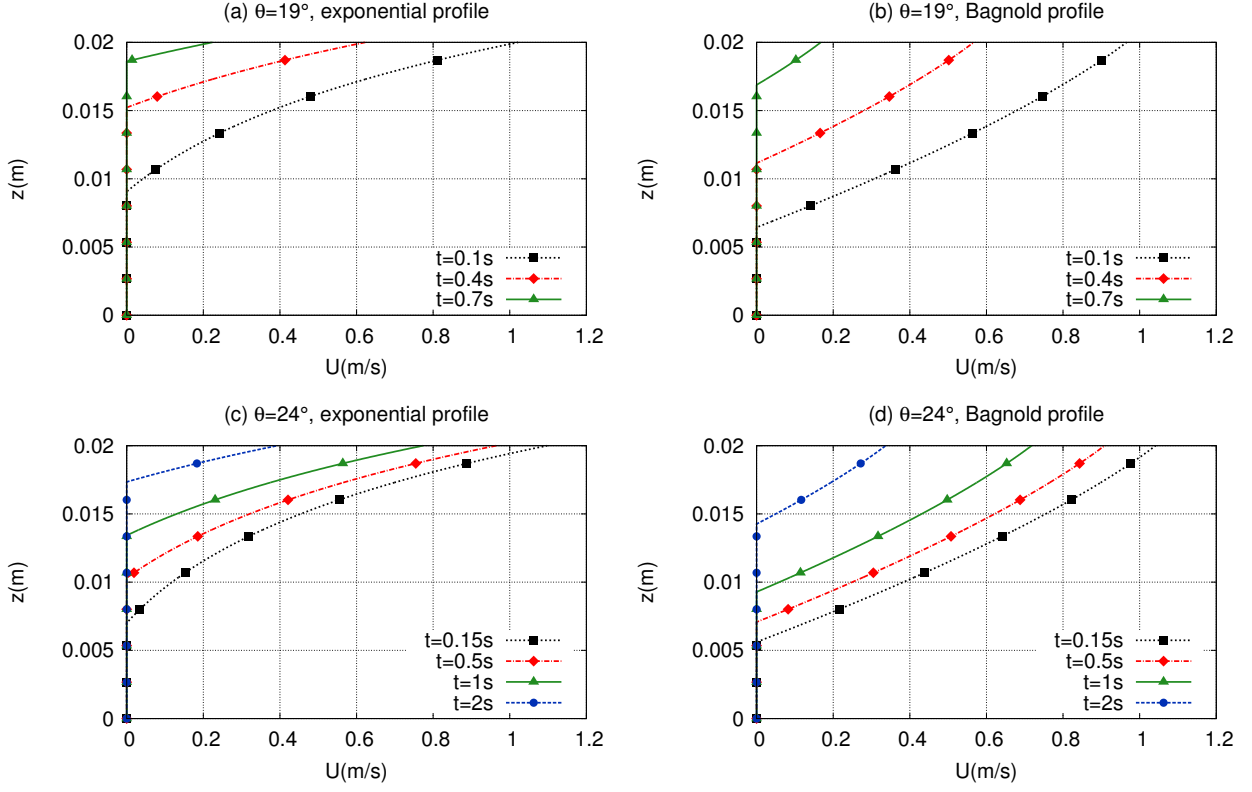


Figure 8: Velocity profiles $U(Z)$ at different times in the inviscid case, with an initially static granular layer of thickness $b^0 = 5\text{mm}$ over an inclined plane of slope (a,b) $\theta = 19^\circ$ and (c,d) $\theta = 24^\circ$, using (a,c) an exponential and (b,d) a Bagnold initial velocity profile.

3.3 Results and comparison with experiments

The profiles of $b(t)$ are plotted in Figure 6, and the profiles of $U(Z)$ are plotted in Figures 7 and 8. The evolution of the static/flowing interface $b(t)$ obtained from the analytical solution (Figure 6) reproduces partly the experimental observations (Figure 3). The shape of $b(t)$ is directly related to the velocity profile, as demonstrated by equation (2.14). In the analytical solution, depending on the initial velocity profile, the stopping time is in the range 2.75-3s for $\theta = 24^\circ$, 1.35-1.5s for $\theta = 22^\circ$, and 0.75-0.85s for $\theta = 19^\circ$, while $t^{\text{stop}} \simeq 3.4\text{s}$, $t^{\text{stop}} \simeq 1.4\text{s}$, and $t^{\text{stop}} \simeq 0.9\text{s}$ in the experiments, respectively. As a result, the stopping time is well reproduced by the analytical solution, even though its strong increase for $\theta = 24^\circ$ is underestimated in the analytical solution. On the contrary, the penetration of the static/flowing interface within the initially static bed is not reproduced by the analytical solution, that only predicts a rising of the static/flowing interface up to the free surface at all times.

The decrease of the velocity with time is quite well reproduced up to about 0.8s. Indeed, in the analytical solution, the velocity profiles maintain almost the same shape while the maximum velocity decreases, as observed in the experiments. The decrease of the maximum velocity in the experiments and in the analytical solution are very similar (Figures 4 and 8). At later times ($t \geq 1\text{s}$) and at $\theta = 22^\circ$ and $\theta = 24^\circ$, the experiments show a clear change of the velocity profile (see Figure 4c at $t = 1\text{s}$ and $t = 2\text{s}$) that is not reproduced by the constant shape of the velocity profiles predicted by the analytical solution. Furthermore, the maximum velocity decreases much faster in the experiments. In the experiments, the velocity profiles seem to be closer to linear for smaller slopes ($\theta = 19^\circ$ and $\theta = 22^\circ$) and more exponential for $\theta = 24^\circ$. Referring to equation (3.5) and Figure 6, this may explain why $b(t)$ has an exponential shape at $\theta = 24^\circ$, while it is closer to linear for smaller slope

angles (Figure 3).

4 Numerical study of the viscous model

In this section, we first describe the methodology to obtain a numerical solution to the simplified model (2.4), (2.5), (2.6) with viscosity $\nu > 0$, and we perform a scale analysis of the main features of the transient regime. Then, we compare the results obtained with constant and uniform source term S given by (3.3) to the experimental data.

4.1 Discretization by moving interface

The first numerical method, described in more detail in [Lusso, 2013], hinges on the rewriting of (2.4), (2.5), (2.6) in a normalized coordinate $0 \leq Y \leq 1$. We perform the change of variables

$$t = \tau, \quad Z = b(\tau) + (h - b(\tau))Y, \quad (4.1)$$

that leads to the differential relations $\partial_\tau = \partial_t + \dot{b}(\tau)(1 - Y)\partial_Z$ and $\partial_Y = (h - b(\tau))\partial_Z$. Here, ∂_t and ∂_τ denote the differentiation with respect to time at constant Z and Y , respectively. The change of variables (4.1), and hence the discretization method presented in this subsection, is appropriate as long as there is a flowing layer. Another discretization method dealing with the stopping phase when $b(t)$ reaches the total height h , is presented in Subsection 4.3. The discretization method considered in this subsection has the advantage of tracking explicitly the position of the static/flowing interface, while the method of Subsection 4.3 requires a post-processing to evaluate the interface position.

Using the change of variables (4.1), equation (2.4) is transformed into

$$\partial_\tau U - \dot{b} \frac{1 - Y}{h - b} \partial_Y U + S - \frac{\nu}{(h - b)^2} \partial_{YY}^2 U = 0 \quad \text{for all } Y \in (0, 1), \quad (4.2)$$

and the boundary conditions (2.5) into

$$U = 0 \quad \text{at } Y = 0, \quad (4.3a)$$

$$\nu \partial_Y U = 0 \quad \text{at } Y = 0, \quad (4.3b)$$

$$\nu \partial_Y U = 0 \quad \text{at } Y = 1. \quad (4.3c)$$

We split the space domain $(0, 1)$ in n_Y cells of length ΔY with $n_Y \Delta Y = 1$, and denote by $Y_j = (j - 1/2)\Delta Y$, for all $j = 1 \dots n_Y$ the center of the cells. The discrete times t^n , for $n \geq 0$ are related by $t^{n+1} = t^n + \Delta t^n$, where Δt^n is the time step (chosen according to the CFL condition (4.7) below) and $t^0 = 0$. We write a finite difference scheme for the discrete unknowns $U_j^n \simeq U(t^n, Y_j)$ and $b^n \simeq b(t^n)$, for all $j = 1 \dots n_Y$ and all $n \geq 1$, using the initial conditions on U^0 (and b^0) to initialize the scheme. For all $n \geq 0$, given $(U_j^n)_{1 \leq j \leq n_Y}$ and b^n , the equations to compute $(U_j^{n+1})_{1 \leq j \leq n_Y}$ and b^{n+1} are

$$\frac{U_j^{n+1} - U_j^n}{\Delta t^n} - \frac{(1 - Y_j)}{h - b^n} a_j^{n+\frac{1}{2}} + S(t^n, Y_j) - \frac{\nu}{(h - b^n)^2} \frac{U_{j+1}^{n+1} + U_{j-1}^{n+1} - 2U_j^{n+1}}{\Delta Y^2} = 0, \quad (4.4)$$

for all $j = 1 \dots n_Y$, with

$$a_j^{n+\frac{1}{2}} = \begin{cases} \dot{b}^{n+\frac{1}{2}} \frac{U_j^n - U_{j-1}^n}{\Delta Y} & \text{if } \dot{b}^{n+\frac{1}{2}} \leq 0, \\ \dot{b}^{n+\frac{1}{2}} \frac{U_{j+1}^n - U_j^n}{\Delta Y} & \text{if } \dot{b}^{n+\frac{1}{2}} \geq 0, \end{cases} \quad \text{with } \dot{b}^{n+\frac{1}{2}} = \frac{b^{n+1} - b^n}{\Delta t^n}, \quad (4.5)$$

together with the boundary conditions

$$U_0^{n+1} = -U_1^{n+1}, \quad (4.6a)$$

$$U_0^{n+1} = U_1^{n+1}, \quad (4.6b)$$

$$U_{n_Y+1}^{n+1} = U_{n_Y}^{n+1}. \quad (4.6c)$$

Equations (4.6a) and (4.6c) are used to provide the ghost values U_0^{n+1} and $U_{n_Y+1}^{n+1}$ involved in (4.4) for $j = 1$ and $j = n_Y$, while equation (4.6b) is used to determine b^{n+1} as described below. We observe that in (4.4), the diffusive term is treated implicitly in time, while the first-order derivative of U is treated explicitly using upwinding. As a result, we impose the CFL condition

$$\frac{\Delta t^n |\dot{b}^{n+\frac{1}{2}}|}{h - b^n} \leq \Delta Y. \quad (4.7)$$

This CFL condition is evaluated approximately using the value $\dot{b}^{n-\frac{1}{2}}$ from the previous time step, since $\dot{b}^{n+\frac{1}{2}}$ is unknown at the beginning of the time step; for $n = 0$, the value 0 is used (hence, no CFL condition is initially enforced, but the time step is taken small enough). Typical values are $\Delta t^0 = 10^{-4}$ s for the initial time step, and $\Delta Y = 10^{-4}$.

The solution to (4.4), (4.5), (4.6) is obtained as follows. We can solve the system (4.4) together with the boundary conditions (4.6a), (4.6c), for any value of b^{n+1} to evaluate the right-hand side (recall that the advective derivative is treated explicitly). This leads to a tridiagonal linear system whose system matrix results only from the time derivative and the diffusive terms. This matrix, which is diagonally dominant, has an inverse with nonnegative entries. Thus, the solution $(U_j^{n+1})_{1 \leq j \leq n_Y}$ can be expressed linearly with nonnegative coefficients in terms of the coefficients $(a_j^{n+1/2})_{1 \leq j \leq n_Y}$ which appear on the right-hand side and which depend on the still unknown interface position b^{n+1} . According to (4.5) and since U_j^n is nondecreasing with respect to j , U_j^{n+1} is thus, for all $j = 1 \dots n_Y$, a nondecreasing continuous and piecewise linear function of b^{n+1} , with two different formulae corresponding to whether b^{n+1} is greater or smaller than b^n . In particular, the remaining boundary condition (4.6b), which is equivalent to $U_1^{n+1} = 0$ owing to (4.6a), determines a unique solution b^{n+1} , see Figure 9. The value of b^{n+1} can be computed explicitly by solving twice the linear system with two different right-hand sides and using linear interpolation. The first solve uses the right-hand side evaluated with the temporary value b^n for b^{n+1} , yielding a temporary value for U_1^{n+1} ; if the obtained value is negative (left panel of Figure 9), the second solve is performed using the value h for b^{n+1} , otherwise, the value 0 is used (right panel of Figure 9). Once b^{n+1} is known, we recover the entire profile U_j^{n+1} for all $j = 1 \dots n_Y$ by linear interpolation.

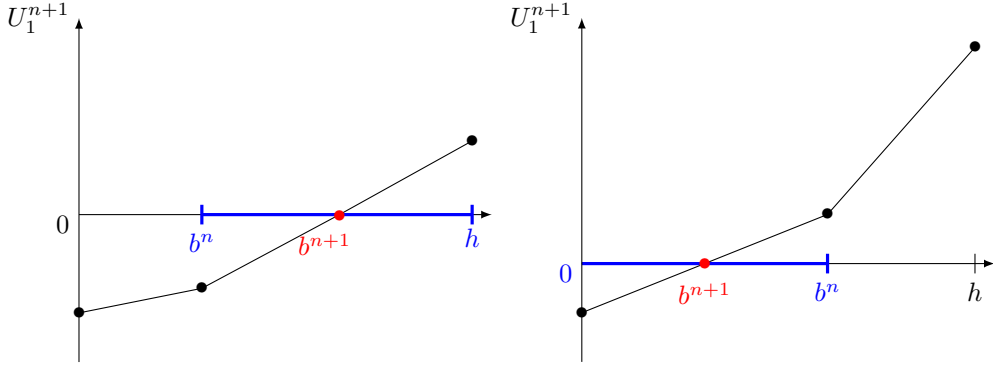


Figure 9: Velocity U_1^{n+1} versus b^{n+1} . The chosen value for b^{n+1} is determined by the intersection of the curve with the horizontal axis.

4.2 Scales in the transient regime

We assume that the source term S is constant. Then, the solution to the viscous model (2.4), (2.5), (2.6) depends on the constant S , the total width h , the viscosity ν , the initial width of the static layer b^0 , and the initial velocity profile $U^0(Z)$. We introduce non-dimensional quantities, denoted by hats, as

$$t = \tau \hat{t}, \quad Z = l \hat{Z}, \quad h = l \hat{h}, \quad b = l \hat{b}, \quad U = u \hat{U}, \quad (4.8)$$

with τ a time scale, l a space scale, and $u = l\alpha_1$ where α_1 is the order of magnitude of the initial shear rate. In order to write (2.4) in non-dimensional form, we take

$$l = \nu \frac{\alpha_1}{S}, \quad \tau = \frac{l^2}{\nu} = \nu \frac{(\alpha_1)^2}{S^2}. \quad (4.9)$$

The dimensionless equation is then

$$\partial_t \hat{U} + 1 - \partial_{\hat{Z}}^2 \hat{U} = 0 \quad \text{for all } \hat{Z} \in (\hat{b}, \hat{h}),$$

with boundary conditions $\hat{U} = \partial_{\hat{Z}} \hat{U} = 0$ at $\hat{Z} = \hat{b}$, and $\partial_{\hat{Z}} \hat{U} = 0$ at $\hat{Z} = \hat{h}$. If we take a linear initial velocity profile, this non-dimensional solution \hat{U} depends only on $\hat{h} = h/l$ and $\hat{b}^0 = b^0/l$. Actually, since the problem is invariant by translation in Z , the solution depends only on $(h - b^0)/l$.

Numerical investigations for constant source S using the scheme described in Subsection 4.1 show the behavior illustrated in Figure 10. The static/flowing interface position $b(t)$ first decreases until a time t^c and attains a minimal value b^{\min} (starting phase). Then, $b(t)$ increases, and (if h is sufficiently large) reaches an asymptotic regime with upward velocity \dot{b}^∞ (stopping phase), before fully stopping at attaining h .

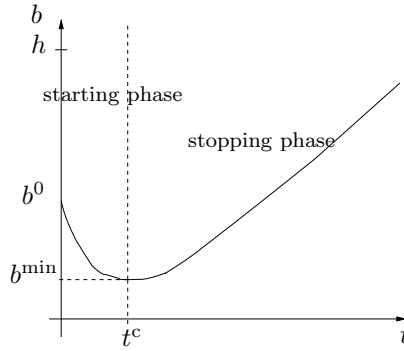


Figure 10: Evolution of the thickness of the static/flowing interface as a function of time.

According to the above scaling analysis, if the velocity profile is initially linear with shear α_1 , and if

$$\frac{h - b^0}{l} = \frac{(h - b^0)S}{\nu\alpha_1} \gg 1, \quad (4.10)$$

the quantities t^c , $b^0 - b^{\min}$, \dot{b}^∞ are proportional to τ , l , l/τ , respectively. We obtain the proportionality factors from the numerical simulation as

$$t^c = 0.15\nu \frac{(\alpha_1)^2}{S^2}, \quad b^0 - b^{\min} = 0.43\nu \frac{\alpha_1}{S}, \quad \dot{b}^\infty = 0.95 \frac{S}{\alpha_1}. \quad (4.11)$$

Note the dependency in the ratio α_1/S , which is due to the homogeneity of the problem (2.4), (2.5) with respect to (U, S) (multiplying (U, S) by a positive constant gives again a solution, with b unmodified).

4.3 Discretization by optimality condition

The second numerical method for solving (2.4), (2.5), (2.6) with positive viscosity $\nu > 0$ is also described in [Lusso, 2013]. It uses a formulation as an optimal problem set on the whole interval $(0, h)$ which is valid under assumption (2.8), i.e.,

$$\begin{cases} \min(\partial_t U + S - \nu \partial_{ZZ}^2 U, U) = 0 & \text{for all } Z \in (0, h), \\ \partial_Z U = 0 & \text{at } Z = h, \\ U = 0 & \text{at } Z = 0, \end{cases} \quad (4.12)$$

where we consider a no-slip boundary condition at the bottom. Note that this condition becomes relevant whenever the static/flowing interface reaches the bottom, a situation encountered in our simulations as reflected in Figure 11c. In (4.12), the static/flowing interface position $b(t)$ no longer appears explicitly, but has to be deduced from the velocity profile as

$$b(t) = \sup \{Z_0 \in [0, h] \text{ such that } U(t, Z) = 0 \text{ for all } Z \in [0, Z_0]\}. \quad (4.13)$$

We split the space domain $(0, h)$ in n_Z cells of length ΔZ with $n_Z \Delta Z = h$, and denote by $Z_j = (j - 1/2)\Delta Z$, for all $j = 1 \dots n_Z$, the center of the cells. The discrete times t^n , for all $n \geq 0$ are related by $t^{n+1} = t^n + \Delta t^n$, where Δt^n is the time step (chosen according to the CFL condition (4.16) below) and $t^0 = 0$. We discretize the problem (4.12) using a finite difference scheme by writing for the discrete unknowns $U_j^n \simeq U(t^n, Z_j)$

$$\min \left(\frac{U_j^{n+1} - U_j^n}{\Delta t^n} + S(t^n, Z_j) - \nu \frac{U_{j+1}^n + U_{j-1}^n - 2U_j^n}{\Delta Z^2}, U_j^{n+1} \right) = 0 \quad (4.14)$$

for all $j = 1 \dots n_Z$. The boundary conditions, which are discretized as $U_{n_Z+1}^n = U_{n_Z}^n$ at the free surface ($Z = h$) and as $U_0^n = -U_1^n$ at the bottom ($Z = 0$), are used to provide the ghost values involved in the discretization of the diffusive term. The problem (4.14) is solved in two steps as

$$\frac{U_j^{n+1/2} - U_j^n}{\Delta t^n} + S(t^n, Z_j) - \nu \frac{U_{j+1}^n + U_{j-1}^n - 2U_j^n}{\Delta Z^2} = 0, \quad U_j^{n+1} = \max(U_j^{n+1/2}, 0). \quad (4.15)$$

Owing to the explicit discretization of the diffusive term, we use the CFL condition

$$2\nu \frac{\Delta t^n}{\Delta Z^2} \leq 1. \quad (4.16)$$

We could also consider an implicit discretization to avoid any CFL condition, but each time step would be more computationally demanding. Finally, the thickness of the static layer is evaluated as

$$b^n = \max \{j \in \{1 \dots n_Z\} \text{ such that } U_k^n = 0 \text{ for all } k \in \{1 \dots j\}\} \times \Delta Z. \quad (4.17)$$

However, in order to avoid that b^n is influenced by small values of U , we prefer to use

$$b^n = (k^n - 1)\Delta Z, \quad k^n = \min \{j \in \{1, \dots, n_Z\} \text{ such that } U_j^n \geq C_0 \Delta Z^2\}, \quad (4.18)$$

where C_0 is an appropriate constant of the order of S/ν , see (2.12).

4.4 Results and comparison with experiments

We consider the case of a constant and uniform source term of the form (3.3). The case of a linear initial velocity profile is simulated using different values of the viscosity ν and slope angles θ . As discussed in Subsection 4.2, the static/flowing interface always penetrates the initially static layer, in contrast to what has been observed for the inviscid case, within a length $b^0 - b^{\min}$ proportional to ν , according to (4.11). In other words, the flow excavates the static bed. However, for $\nu < 10^{-5} \text{m}^2 \cdot \text{s}^{-1}$, the penetrating length is too small to be observable. For $\nu = 10^{-5} \text{m}^2 \cdot \text{s}^{-1}$ (Figure 11a), $b^0 - b^{\min} = 8.10^{-4} \text{m}$ for $\theta = 24^\circ$ (with $t^c = 5.10^{-2} \text{s}$), and $b^0 - b^{\min} = 2.10^{-4} \text{m}$ for $\theta = 19^\circ$ (with $t^c = 4.10^{-3} \text{s}$). Thus, the static/flowing interface penetrates only slightly within the initially static layer. As the viscosity increases (Figure 11b), the static/flowing interface $b(t)$ penetrates deeper into the initially static layer and even reaches the bottom for $\nu = 10^{-4} \text{m}^2 \cdot \text{s}^{-1}$ at $\theta = 24^\circ$ (Figure 11c). The results that better reproduce the experimental observation for the penetration of $b(t)$ within the initially static layer are obtained with $\nu \simeq 5.10^{-5} \text{m}^2 \cdot \text{s}^{-1}$. In good agreement with the experiments, the simulations with viscosity predict that the static/flowing interface sinks deeper within the

initially static layer and for a longer time t^c when the slope angle increases. Furthermore, the values of $b(t)$ and t^c are in reasonable agreement with those observed experimentally (Figures 3 and 11b and Figure 17 of [Farin et al., 2014]).

Qualitatively similar results are obtained using different initial velocity profiles (Figure 13). However, the shape of $b(t)$ is affected by the choice for the initial velocity profile. As an example, for an exponential initial velocity profile with $\theta = 24^\circ$ and $\nu = 5.10^{-5} \text{m}^2.\text{s}^{-1}$, the static/flowing interface $b(t)$ stagnates at an almost constant position for the first 0.5s, contrary to the case of a linear initial velocity profile (Figures 11b and 13b).

The convex shape of $b(t)$ during the migration of the static/flowing interface up to the free surface obtained in the viscous case is very different from the observation and from that obtained in the inviscid case, which predicted a linear shape related to the linear initial velocity profile. In the viscous case, the time evolution of $b(t)$ and of the velocity profile $U(t, Z)$ are not so obviously related to the shape of the initial velocity profile, as shown for example on Figure 13 for $\theta = 24^\circ$. The velocity profiles in the viscous case are also very different from those in the inviscid case. Whatever the shape of the initial velocity profile, at later time, the velocity profiles exhibit an exponential-like tail near the static/flowing interface, similar to that observed experimentally. They also exhibit a convex shape near the free surface which can be observed in some experimental velocity profiles, but not always and not as marked (e.g., Figure 4c). While the maximum velocity decreases too fast at $t = 0.5\text{s}$ and $\theta = 24^\circ$ compared to the experiments and to the inviscid case, the velocity is much closer to the experiments at $t = 1\text{s}$ than in the inviscid case (Figure 4c and Figure 12c). For $\theta = 19^\circ$ and $\theta = 22^\circ$, the viscous case overestimates the decrease in velocity at time $t = 0.7\text{s}$. Finally, the stopping time of the whole granular layer is smaller for viscous than for inviscid flow, whatever the shape of the initial velocity profile. Recalling that the stopping time in the inviscid case is given by $t_{\nu=0}^{\text{stop}} = U^0(h)/S$, we can study numerically the difference ($t_{\nu=0}^{\text{stop}} - t_\nu^{\text{stop}}$), where t_ν^{stop} denotes the stopping time in the viscous case. Our numerical simulations show that this difference depends rather mildly on the viscosity (Figure 14 where the slope of the curves suggests a behavior of this difference close to $\nu^{1/4}$ for the present parameters). In any case, the presence of viscosity diminishes the stopping time. Furthermore, the stopping time in the viscous case is significantly smaller than in the experiments.

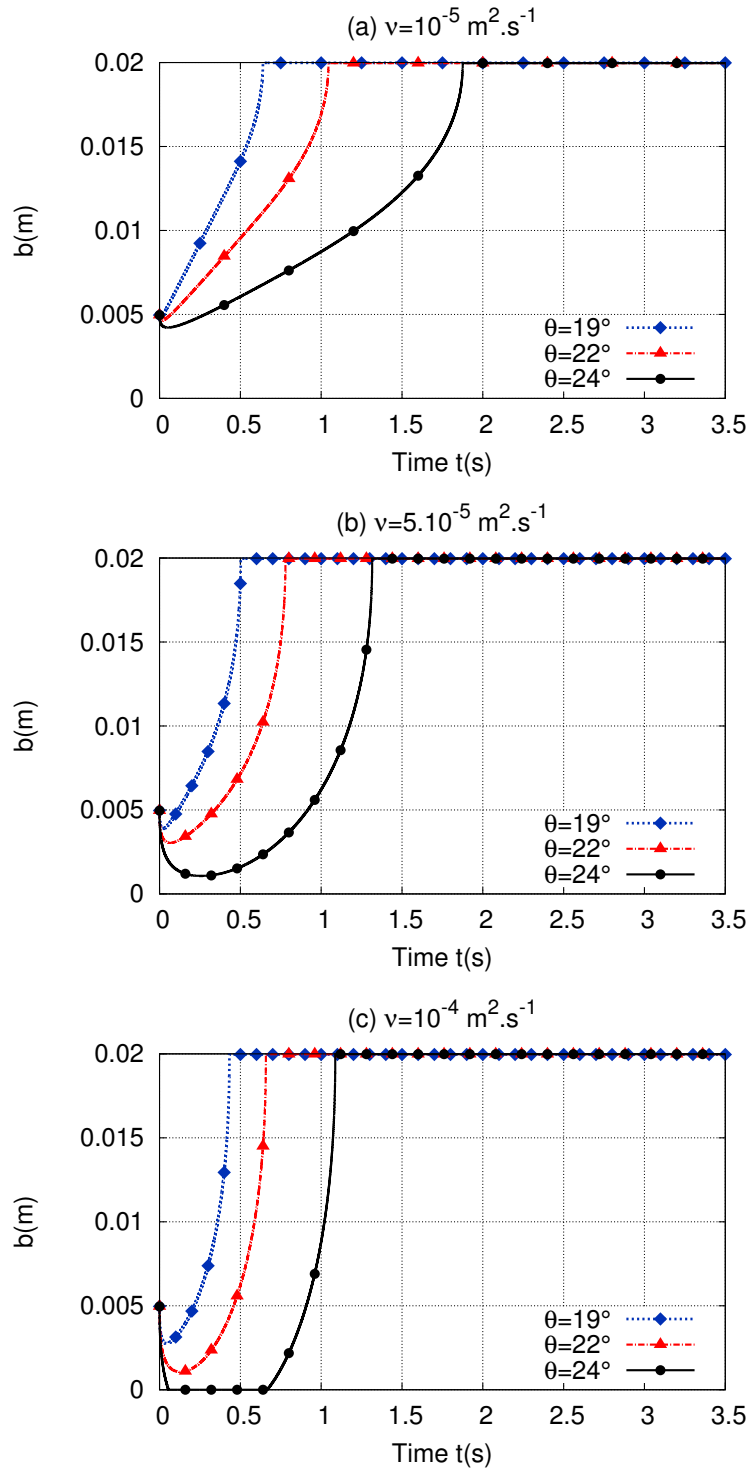


Figure 11: Static/flowing interface b as a function of time t for different slope angles using a linear velocity profile, and different viscosities (a) $\nu = 10^{-5} \text{ m}^2 \cdot \text{s}^{-1}$, (b) $\nu = 5 \cdot 10^{-5} \text{ m}^2 \cdot \text{s}^{-1}$, and (c) $\nu = 10^{-4} \text{ m}^2 \cdot \text{s}^{-1}$.

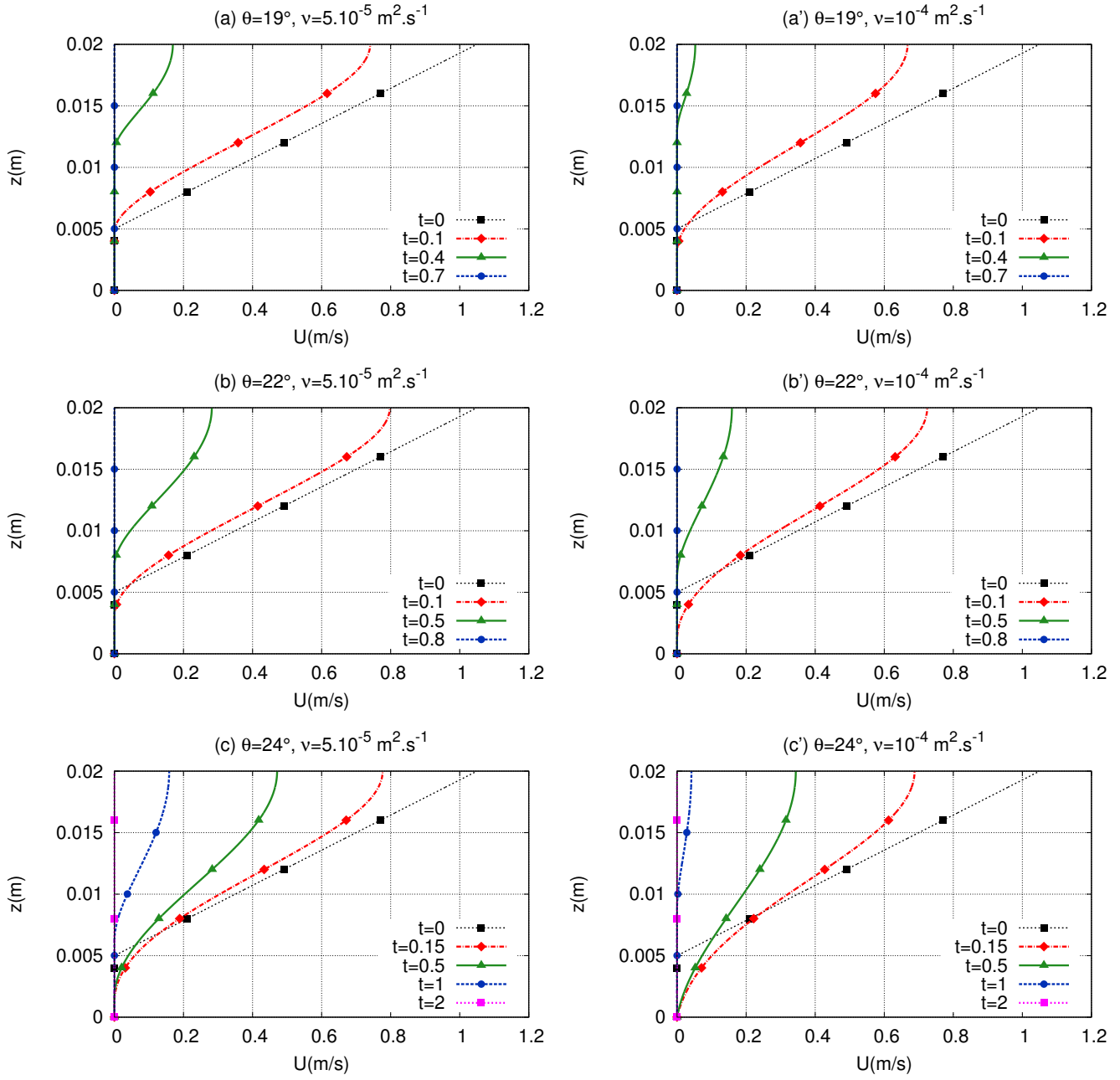


Figure 12: Velocity profiles $U(Z)$ at different times, with a linear velocity profile, for two different viscosities (a-b-c) $\nu = 5.10^{-5} \text{ m}^2 \cdot \text{s}^{-1}$ and (a'-b'-c') $\nu = 10^{-4} \text{ m}^2 \cdot \text{s}^{-1}$, and for the slope angles (a-a') $\theta = 19^\circ$, (b-b') $\theta = 22^\circ$, and (c-c') $\theta = 24^\circ$.

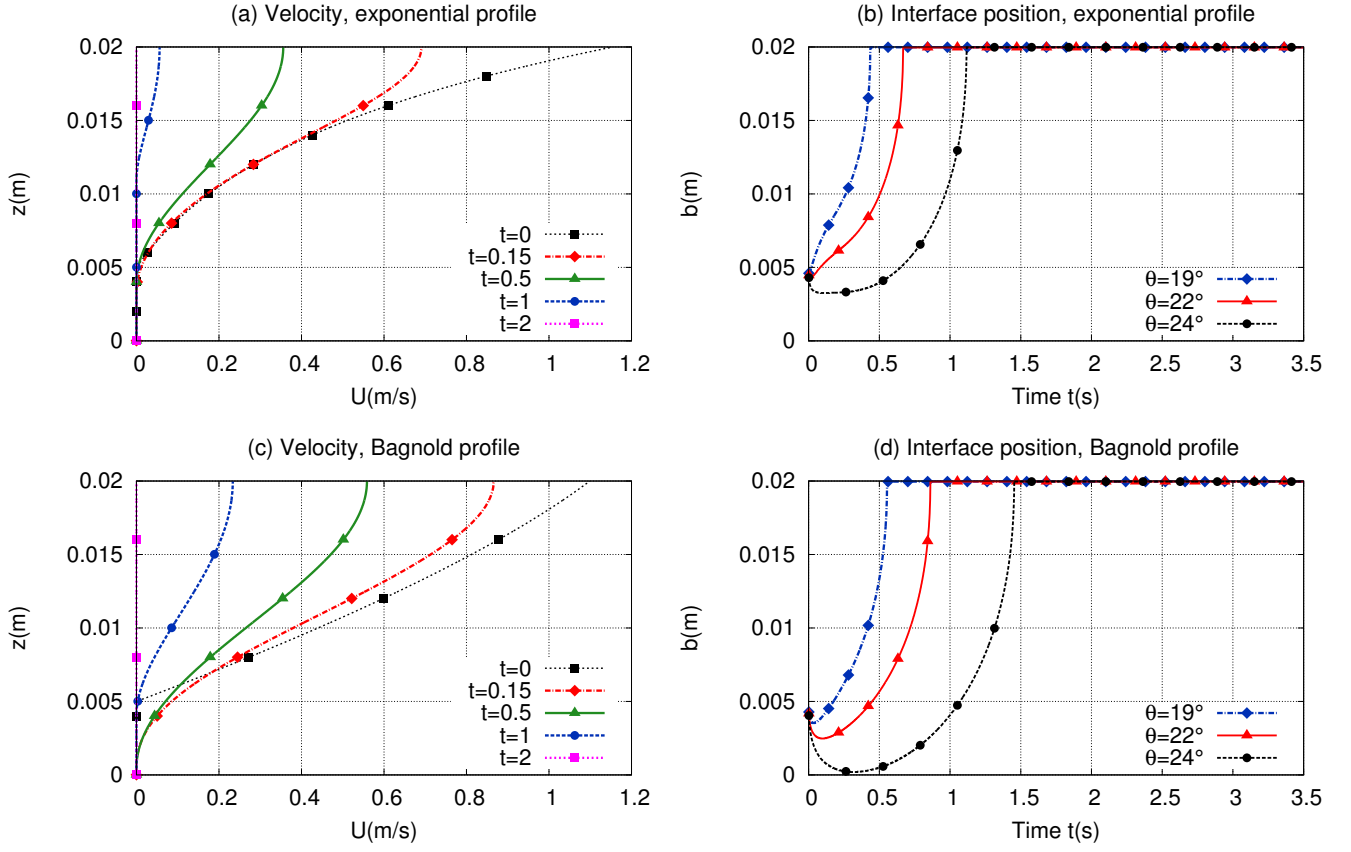


Figure 13: (left) Velocity profiles $U(Z)$ and (right) evolution of the thickness of the static/flowing interface b , with an inclined plane of slope $\theta = 24^\circ$ and a viscosity $\nu = 5.10^{-5} \text{m}^2 \cdot \text{s}^{-1}$, using (a-b) an exponential and (c-d) a Bagnold initial velocity profile.

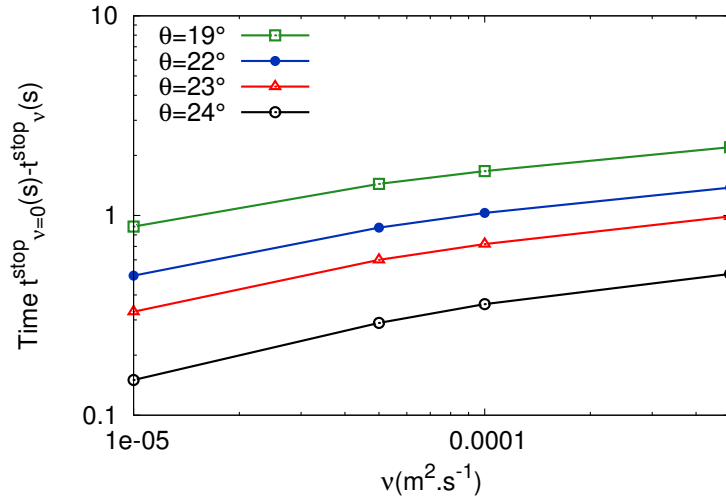


Figure 14: $t_{\nu=0}^{\text{stop}} - t_{\nu}^{\text{stop}}$ with respect to the viscosity in log scale.

5 Discussion and conclusion

We have presented here a 1D (in the direction normal to the flow) thin layer model based on the description of a granular material by the Drucker–Prager yield stress rheology. We have compared its solution in the inviscid and viscous cases to granular flow experiments over an inclined static layer of grains. In this model the flow thickness is constant. The analytical solution in the inviscid case and the numerical results in the viscous case reproduce quantitatively some essential features of the change in time of the velocity, of the static/flowing interface, and of the stopping time of the granular mass, even though in the experiments the flow thickness is not perfectly uniform and the initial velocity profile changes with slope angle and flow thickness.

The analytical solution in the inviscid case shows that the evolution of the static/flowing interface is proportional to the source term and inversely proportional to the velocity profile (equation (2.14)). In the viscous case, the analysis of the model shows that the evolution of the interface is related to the viscosity, to the source term, and to the first and third derivative of the source term and of the velocity, respectively (equation (2.13)). While in the inviscid case the shape of the initial velocity profile is preserved at all times according to (3.4), in the viscous case an exponential-like tail near the static/flowing transition and a convex shape near the free surface develop. The viscous contribution makes it possible for the static/flowing interface to initially penetrate within the static layer (which is eroded) as observed in the experiments, contrary to the inviscid case.

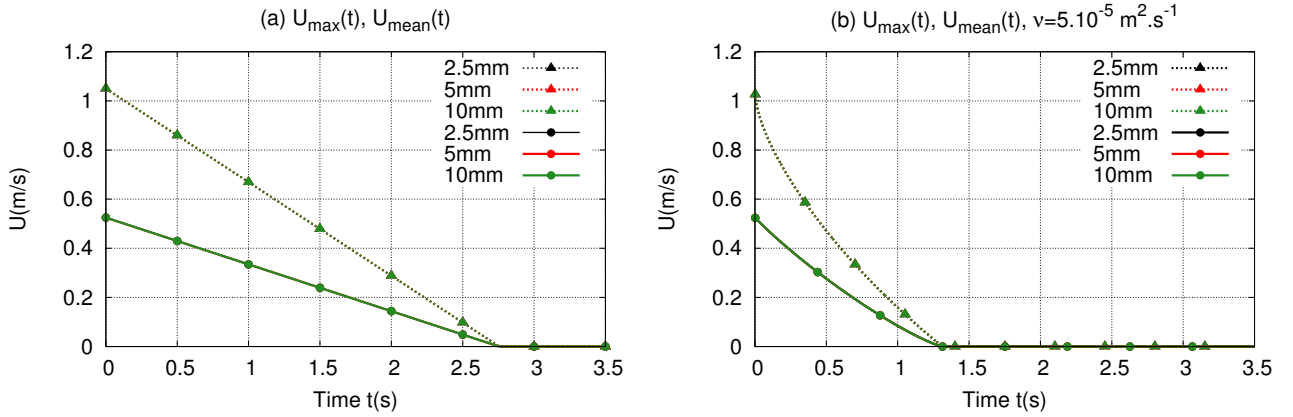


Figure 15: Maximum velocity $U_{\max}(t)$ (dotted lines) and mean velocity $U_{\text{mean}}(t)$ (full lines) predicted by the present simplified model using a linear initial velocity profile over an inclined plane of slope $\theta = 24^\circ$, in the inviscid case (a) and for $\nu = 5.10^{-5} \text{ m}^2 \cdot \text{s}^{-1}$ (b), with different thickness of initially static granular layer.

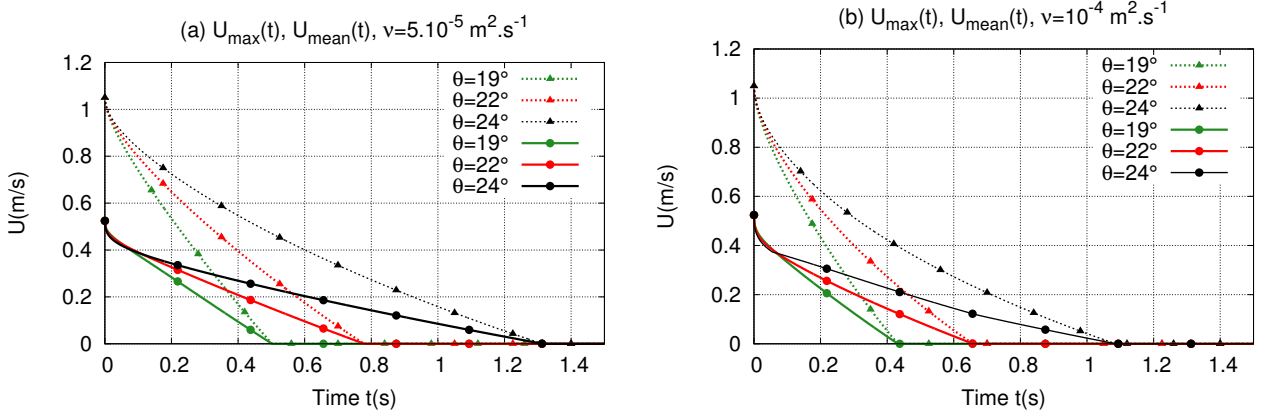


Figure 16: Maximum velocity $U_{\max}(t)$ (dotted lines) and mean velocity $U_{\text{mean}}(t)$ (full lines) predicted by the simplified model at different slope angles, with a linear velocity profile and an initially static granular layer of thickness $b^0 = 5\text{mm}$, for two different viscosities (a) $\nu = 5.10^{-5}\text{m}^2\text{s}^{-1}$ and (b) $\nu = 10^{-4}\text{m}^2\text{s}^{-1}$.

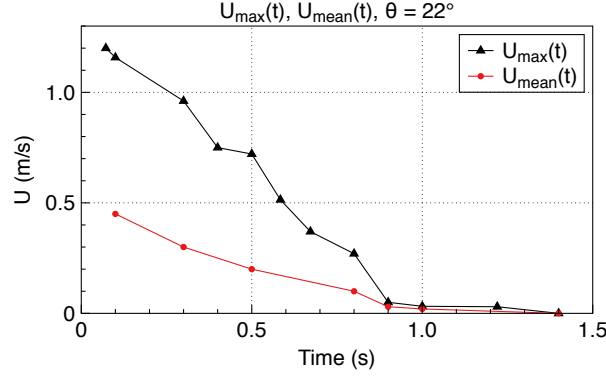


Figure 17: Maximum velocity $U_{\max}(t)$ and mean velocity $U_{\text{mean}}(t)$, with a linear velocity profile measured at $X = 90\text{cm}$ from the gate, in experiments of granular collapse over an initially static granular layer of thickness $b^0 = 5\text{mm}$ and an inclined channel of slope $\theta = 22^\circ$.

One of the important results of this analysis is the explicit expressions obtained from the analytical solution, especially for the time evolution of the static/flowing interface. The analysis shows that the dynamics is controlled by the source term S that is constant when hydrostatic pressure is assumed and when the slope and thickness are supposed to be constant. In that case, $S(t, Z) = S = g \cos \theta (\tan \delta - \tan \theta)$. Comparable results have been obtained from the analytical solution of shallow depth-averaged equations in a granular dam-break (i.e., with non-constant h) [Mangeney et al., 2000; Faccanoni and Mangeney, 2013]. This analytical solution predicts a granular mass front velocity that decreases linearly with time

$$U_f = \max \left(2\sqrt{kgh_0 \cos \theta} - (g \cos \theta (\tan \delta - \tan \theta) t, 0 \right), \quad (5.1)$$

where $k \simeq 0.5$ (see [Mangeney et al., 2010]). Furthermore, the stopping time of the analytical front for the granular dam-break is

$$t_f = 2\sqrt{\frac{k h_0}{g \cos \theta}} \frac{1}{\tan \delta - \tan \theta}. \quad (5.2)$$

Equations (5.1), (5.2) for the front velocity and the stopping time of the front for a depth-averaged model of granular dam-break are very similar to equations (3.4) and (3.6) respectively, found here for the mean velocity of the flow and for the stopping time of the granular layer in the non-averaged case and without viscosity. In the experiments of [Farin et al., 2014], $2\sqrt{kg h_0 \cos \theta} \simeq 1.6\text{m/s}$ which is of the same order of magnitude as $U_0(h) \simeq 1\text{m/s}$, relating equations (3.6) and (5.2). This suggests that the duration of the granular collapse until the front stops is about the same as the duration of the propagation of the static/flowing interface up to the free surface. This is also in good agreement with experimental observations [e.g., Mangeney-Castelnau et al., 2005; Mangeney et al., 2010]. Another interesting result from our simplified model concerns the mean velocity, calculated by depth-averaging over the flowing layer the velocity $U(t, Z)$, and the maximum velocity. These two quantities are given by

$$U_{\text{mean}}(t) = \frac{1}{h - b(t)} \int_{b(t)}^h U(t, Z) dZ, \quad (5.3a)$$

$$U_{\text{max}}(t) = U(t, h). \quad (5.3b)$$

In the inviscid case with initial linear velocity profile, the mean velocity is linearly decreasing in time with a slope equal to $-S/2$. This type of behavior is also predicted by the shallow depth-averaged granular model (Figure 15a). The maximum velocity exhibits the same linear decrease in time, but with a slope $-S$, since $U_{\text{mean}}(t) = U_{\text{max}}(t)/2$ in the present case. Taking into account the viscosity brings in several interesting new effects. First, this leads to a non-linear decrease of the mean and maximum velocities with time (Figures 15b and 16). Experimental results could be compatible with the inviscid or viscous cases (Figure 17). Incidentally, we observe that in both the inviscid and viscous cases, the mean and maximum velocities are independent of the initial thickness of the static layer b^0 (Figure 15), while the experiments of [Mangeney et al., 2010] suggest a small increase of the front velocity as b^0 increases (see their Figure 11). Another consequence of taking into account the viscosity is that it allows us to reproduce the initial penetration of the static/flowing interface into the static layer (erosion), but, at the same time, leads to underestimating the stopping time. Additionally, the viscous model reproduces better than the inviscid one the exponential-like tail of the velocity profile near the static/flowing interface, but overestimates the convexity of the velocity profile near the free surface. Furthermore, the change of shape of the velocity profile observed in the experiments near the arrest of the whole layer is reproduced in the viscous case contrary to the inviscid case, but the decrease in maximum velocity near the surface is too fast in the viscous case. All these results suggest that (i) the viscosity plays an important role near the static/flowing interface at depth, and in this region a reasonable estimate for the viscosity is $\nu \simeq 5.10^{-5}\text{m}^2.\text{s}^{-1}$ (ii) viscous effects in the experiments seem to be much smaller near the free surface. These observations suggest a non-constant viscosity as proposed in the so-called $\mu(I)$ flow law, where I is the inertial number [e.g., GDR-MiDi, 2004; Silbert et al., 2001; Jop et al., 2005, 2006]. Interestingly, [Ionescu et al., 2014] show that it is possible to use the $\mu(I)$ flow law in granular collapse over inclined planes in order to derive the value of the viscosity. A possible approximation is $\nu = (\mu_2 - \mu) \frac{d}{I_0} \sqrt{p}$, where μ_2 is the friction at large strain rate, d is the grain diameter, $I_0 = 0.279$, and p is the pressure. Here, the hydrostatic pressure $p = g \cos \theta (h - Z)$ makes explicit the variation of the viscosity with respect to the normal variable Z . Taking $\mu_2 = \tan(32^\circ)$, $\mu = \tan(26^\circ)$, $\theta = 22^\circ$, $h = 0.02\text{m}$, $Z = b^0 = 0.005\text{m}$, and from [Farin et al., 2014] $d = 7.10^{-4}\text{m}$, we infer that the viscosity near the static/flowing interface ν is about $10^{-4}\text{m}^2.\text{s}^{-1}$, while it is almost zero at the free surface because the pressure at the surface is almost zero and the shear rate is the largest, which leads to high values of I (see e.g., [Jop et al., 2005]).

While the so-called partial fluidization theory, involving an order parameter to describe the transition between static and flowing material, also reproduces the erosion of the static bed and the velocity profiles obtained here in the viscous case [Mangeney et al., 2007], the Drucker–Prager model used here has the great advantage to involve only two parameters, i.e., the friction coefficient μ and the viscosity ν without any empirical equations for the

time-change of a state parameter. Using a viscosity that depends on the shear rate and the pressure as in the $\mu(I)$ flow law (which has not been done here) would also add more parameters but seems to be necessary to reproduce the flow both near the static/flowing interface and within the developed flow layer, as well as the characteristics of the stopping phase. Another possible approach to introduce more parameters would be to take into account the variations of the source S from (2.3), thereby accounting for the flow-aligned variations and the non-hydrostatic effects. The influence of a Z -dependency of S on the static/flowing interface dynamics and on the erosion process has been studied in [Lusso, 2013].

A challenge is to extend the approach proposed here to 2D and possibly 3D, so as to capture the static/flowing interface in shallow models, as proposed in [Bouchut et al., 2014]. The orders of magnitude assumed there are indeed satisfied in the experiments discussed here, because the typical length is $L = 1\text{m}$, typical time $\tau = 0.33\text{s}$ satisfying $L/\tau^2 = g$, $h = 0.02\text{m}$, $\nu = 5.10^{-5}\text{m}^2.\text{s}^{-1}$, leading to $\varepsilon \equiv h/L = 0.02$, $\tan\delta - \tan\theta = O(\varepsilon)$, and the normalized viscosity $\nu\tau/L^2 \simeq 10^{-5}$ is of the order of ε^2 or ε^3 . The primary models of [Bouchut et al., 2014] lead however to severe nonlinearities, so that these extensions with flow-aligned variations remain challenging to treat numerically.

An important issue is also to summarize the dynamics of the normal velocity profile in a finite number of parameters (e.g., the interface b , the width h , the shear...), in order to keep the computational cost low enough to simulate natural situations.

Acknowledgments

The authors are thankful to Maxime Farin and Olivier Roche for sharing the experimental results presented here, that were extracted from [Farin et al., 2014], to Maxime Farin for helping extract the specific results presented here from these experiments, and to Régis Monneau for stimulating discussions on the discretization by an optimality condition. The authors are also grateful to Eliza Calder, Paddy Smith, and Paul Cole that led the field trip where Figure 1 was taken. This work has been partially funded by the ANR contract ANR-11-BS01-0016 LANDQUAKES, by the Labex Bézout, and by the ERC contract ERC-CG-2013-PE10-617472: ERC SLIDEQUAKES.

References

- C. Berger, B.W. McArdell, and F. Schlunegger. Direct measurement of channel erosion by debris flows, illgraben, switzerland. *J. Geophys. Res.*, 116:F01002, 2011. doi: 10.1029/2010JF001722.
- F. Bouchut and M. Westdickenberg. Gravity driven shallow water models for arbitrary topography. *Commun. Math. Sci.*, 2:359–389, 2004.
- F. Bouchut, A. Mangeney-Castelnau, B. Perthame, and J.-P. Vilotte. A new model of Saint Venant and Savage-Hutter type for gravity driven shallow water flows. *C. R. Math. Acad. Sci. Paris*, 336:531–536, 2003. doi: 10.1016/S1631-073X(03)00117-1.
- F. Bouchut, E.D. Fernández-Nieto, A. Mangeney, and P.-Y. Lagrée. On new erosion models of Savage–Hutter type for avalanches. *Acta Mech.*, 199:181–208, 2008.
- F. Bouchut, I. Ionescu, and A. Mangeney. A shallow model including static-flowing transition for viscoplastic Drucker–Prager materials. 2014.
- S.J. Conway, A. Decaulne, M.R. Balme, J.B. Murray, and M.C. Towner. A new approach to estimating hazard posed by debris flows in the westfjords of iceland. *Geomorphology*, 114: 556–572, 2010.
- G.B. Crosta, S. Imposimato, and D. Roddeman. Numerical modeling entrainment/deposition in rock and debris-avalanches. *Eng. Geol.*, 109:135–145, 2009a.

- G.B. Crosta, S. Imposimato, D. Roddeman Wright, R.Y. Yang, B.H. Xu, and A.B. Yu. Numerical modeling of 2-d granular step collapse on erodible and non-erodible surface. *J. Geophys. Res.*, 114:F03020, 2009b. doi: 10.1029/2008JF001186.
- S. Deboeuf, O. Dauchot, L. Staron, A. Mangeney, and J.-P. Vilotte. Memory of the un-jamming transition during cyclic tiltings of a granular pile. *Phys. Rev. E*, E72:051305, 2005.
- G. Faccanoni and A. Mangeney. Exact solution for granular flows. *Int. J. Num. Anal. Meth. Geomech.*, 37:1408–1433, 2013.
- M. Farin, A. Mangeney, and O. Roche. Fundamental changes of granular flow dynamics, deposition, and erosion processes at high slope angles: insights from laboratory experiments. *J. Geophys. Res. Earth Surf.*, 119:504–532, 2014.
- GDR-MiDi. On dense granular flows. *Eur Phys J E Soft Matter*, 14(4):341–365, 2004.
- O. Hungr, S.G. Evans, M.J. Bovis, and J.N. Hutchinson. Review of the classification of landslides of the flow type. *Environ. Eng. Geosci.*, 7:221–238, 2001.
- I.R. Ionescu, A. Mangeney, F. Bouchut, and O. Roche. Viscoplastic modelling of granular column collapse with pressure and rate dependent viscosity. 2014.
- R.M. Iverson. Elementary theory of bed-sediment entrainment by debris flows and avalanches. *J. Geophys. Res.*, 117:F03006, 2012. doi: 10.1029/2011JF002189.
- R.M. Iverson, M. Reid, M. Logan, R. LaHusen, J.W. Godt, and J. Griswold. Positive feedback and momentum growth during debris-flow entrainment of wet bed sediment. *Nat. Geosci.*, 4:116–121, 2011. doi: 10.1038/NGEO104.
- P. Jop, Y. Forterre, and O. Pouliquen. Crucial role of sidewalls in dense granular flows: consequences for the rheology. *J. Fluid Mech.*, 541:167–192, 2005.
- P. Jop, Y. Forterre, and O. Pouliquen. A constitutive law for dense granular flows. *Nature*, 441:727–730, 2006.
- D.V. Khakhar, A.V. Orpe, P. Andresén, and J.M. Ottino. Surface flow of granular materials: model and experiments in heap formation. *J. Fluid Mech*, 441:225–264, 2001.
- P.-Y. Lagrée, L. Staron, and S. Popinet. The granular column collapse as a continuum: validity of a two-dimensional Navier–Stokes model with a $\mu(i)$ -rheology. *J. Fluid Mech*, 686:378–408, 2011.
- A. Lucas, A. Mangeney, and J.-P. Ampuero. Frictional weakening in landslides on earth and on other planetary bodies. *Nature Communication*, 2014. doi: 10.1038/ncomms4417.
- C. Lusso. *Modélisation numérique des écoulements gravitaires viscoplastiques avec transition fluide/solide*. PhD thesis. Université Paris-Est, Champs-sur-Marne, 2013.
- A. Mangeney, Ph. Heinrich, and R. Roche. Analytical and numerical solution of the dam-break problem for application to water floods, debris and dense snow avalanches. *Pure Appl. Geophys.*, 157:1081–1096, 2000.
- A. Mangeney, L.S. Tsimring, D. Volfson, I.S. Aranson, and F. Bouchut. Avalanche mobility induced by the presence of an erodible bed and associated entrainment. *Geophys. Res. Lett.*, 34:L22401, 2007.
- A. Mangeney, O. Roche, O. Hungr, N. Mangold, G. Faccanoni, and A. Lucas. Erosion and mobility in granular collapse over sloping beds. *JGR-Earth Surface*, 115:F03040, 2010.

- A. Mangeney-Castelnau, F. Bouchut, J.-P. Vilotte, E. Lajeunesse, A. Aubertin, and M. Pirulli. On the use of saint venant equations to simulate the spreading of a granular mass. *J. Geophys. Res.*, 110:B09103, 2005. doi: 10.1029/2004JB003161.
- P. Richard, A. Valance, J.-F. Metayer, P. Sanchez, J. Crassou, M. Louge, and R. Delannay. Rheology of confined granular flows: scale invariance, glass transition, and friction weakening. *Phys. Rev. Lett.*, 101:248002, 2008.
- S.B. Savage and K. Hutter. The motion of a finite mass of granular material down a rough incline. *J. Fluid Mech.*, 199:177–215, 1989. doi: 10.1017/S0022112089000340.
- L.E. Silbert, D. Ertas, G.S. Grest, T.C. Halsey, D. Levine, and S.J. Plimpton. Granular flow down an inclined plane: Bagnold scaling and rheology. *Phys. Rev. E*, 64:051302, 2001. doi: 10.1103/PhysRevE.64.051302.
- B. Sovilla, P. Burlando, and P. Bartelt. Field experiments and numerical modeling of mass entrainment in snow avalanches. *J. Geophys. Res.*, 111:F03007, 2006. doi: 10.1029/2005JF000391.
- N. Taberlet, P. Richard, A. Valance, R. Delannay, W. Losert, J.M. Pasini, and J.T. Jenkins. Super stable granular heap in thin channel. *Phys. Rev. Lett.*, 91:264301, 2003.
- J.T. Weidinger, O. Korup, H. Munack, U. Altenberger, S.A. Dunning, G. Toppelt, and W. Lottermoser. Giant rockslides from the inside. *Earth and Planetary Sci. Lett.*, 389: 62–73, 2014.